© 2015. Published by The Company of Biologists Ltd | Journal of Cell Science (2015) 128, 305–316 doi:10.1242/jcs.158915

RESEARCH ARTICLE

Nuclear pore targeting of the yeast Pom33 nucleoporin depends on karyopherin and lipid binding

Aurélie G. Floch[1,2], David Tareste[1,3], Patrick F. J. Fuchs[1], Anne Chadrin[1,2], Ikrame Naciri[1], Thibaut Léger[4], Gabriel Schlenstedt[5], Benoit Palancade[1,*] and Valérie Doye[1,*,‡]

ABSTRACT

Pom33 is an integral membrane protein of the yeast nuclear pore complex (NPC), and it is required for proper NPC distribution and assembly. To characterize the Pom33 NPC-targeting determinants, we performed immunoprecipitation experiments followed by mass spectrometry analyses. This identified a new Pom33 partner, the nuclear import factor Kap123. *In vitro* experiments revealed a direct interaction between the Pom33 C-terminal domain (CTD) and Kap123. *In silico* analysis predicted the presence of two amphipathic α-helices within Pom33-CTD. Circular dichroism and liposome co-flotation assays showed that this domain is able to fold into α-helices in the presence of liposomes and preferentially binds to highly curved lipid membranes. When expressed in yeast, under conditions abolishing Pom33-CTD membrane association, this domain behaves as a Kap123-dependent nuclear localization signal (NLS). Although deletion of Pom33 C-terminal domain (Pom33$^{\Delta CTD}$–GFP) impaired Pom33 stability and NPC targeting, mutants affecting either Kap123 binding or the amphipathic properties of the α-helices did not display any detectable defect. However, combined impairment of lipid and Kap123 binding affects targeting of Pom33 to NPCs. These data highlight the requirement of multiple determinants and mechanisms for proper NPC localization of Pom33.

KEY WORDS: Nuclear pore complex, NPC, Integral membrane protein, Karyopherin, Amphipathic helix, NPC targeting, NPC distribution, TMEM33 family

INTRODUCTION

In eukaryotes, the nuclear envelope segregates the nuclear from the cytoplasmic contents. Most exchanges between these two compartments take place through nuclear pore complexes (NPCs), which are megadalton-size protein assemblies composed of ~30 distinct proteins (nucleoporins, Nups), each present in multiple copies per NPC (reviewed in Aitchison and Rout, 2012; Floch et al., 2014). Although small molecules can freely pass through the NPCs, large macromolecules undergo highly selective nuclear import and/or export processes. The major route for nuclear protein transport involves signaling sequences that are recognized by specific nuclear transport receptors termed karyopherins (Kaps). For nuclear protein import, a variety of nuclear localization signals (NLSs) are recognized by a subset of Kaps called importins (Chook and Süel, 2011). Proteins containing a 'classical' nuclear localization signal (cNLS, typically a short basic sequence or two basic sequences separated by a linker) are recognized by an importin-α–importin-β heterodimer (Kap60–Kap95 in budding yeast). However, most importin-β proteins (including Kap95 in some cases) bind directly to their cargoes through specific NLSs (Marfori et al., 2011; Ptak and Wozniak, 2014). Although some NLSs are recognized by a unique dedicated importin-β, there can be a strong redundancy between the various importin-β family members (10 in budding yeast) (Tran et al., 2007; Fries et al., 2007). The targeting and translocation of Kap–cargo complexes through the ~40-nm wide central NPC channel involve interactions of Kap-β proteins with the unstructured phenylalanine-glycine (FG) repeat sequences present in multiple nucleoporins (FG-Nups) (reviewed in Terry and Wente, 2009). In the nucleus, interaction of importin-β proteins with the small GTPase Ran (Gsp1 and Gsp2 in budding yeast) in its GTP-bound form (Ran-GTP) then leads to the release of the import cargoes thereby ensuring the directionality of transport (reviewed in Conti et al., 2006).

To perform this crucial function as gatekeepers between the nucleus and the cytoplasm, NPCs have to be properly anchored at the points of fusion between the outer and inner nuclear membranes (ONM and INM, respectively) of the nuclear envelope. The corresponding pore membrane domain is a specialized and inherently highly curved area of the nuclear envelope, into which a few integral pore membrane nucleoporins (Poms) are embedded. There are three Poms in mammals (Pom121, gp210 and Ndc1) and four in the budding yeast *Saccharomyces cerevisiae* (Pom34, Pom152, Ndc1 and Pom33), the first three of which associate to form the transmembrane NPC ring (Onischenko et al., 2009). In addition to these transmembrane proteins, several Nups or NPC-associated proteins contain non-integral membrane-binding modules that might also contribute to the anchoring and/or assembly of NPCs within the nuclear envelope. In particular, ALPS motifs (amphipathic lipid-packing sensor, first described in the COPI-coat assembly protein ArfGAP1) have been predicted in several Nups (Drin et al., 2007; Kim et al., 2014). In the case of human Nup133, this domain was demonstrated to bind to curved membranes *in vitro* and to contribute to Nup133 recruitment to NPCs during interphase (Drin et al., 2007; Doucet et al., 2010). In addition, a conserved C-terminal membrane-binding amphipathic α-helix within mammalian Nup53 has been demonstrated to have

[1]Institut Jacques Monod, UMR 7592 CNRS, Université Paris Diderot, Sorbonne Paris Cité, F-75205 Paris, France. [2]Ecole Doctorale Gènes Génomes Cellules, Université Paris Sud, F-91405 Orsay, France. [3]Membrane Traffic in Health & Disease, INSERM ERL U950, 75013 Paris, France. [4]Proteomic facility, Institut Jacques Monod, F-75205 Paris, France. [5]Universität des Saarlandes, Medizinische Biochemie und Molekularbiologie, D-66421 Homburg, Germany. *These authors contributed equally to this work

‡Author for correspondence (doye.valerie@ijm.univ-paris-diderot.fr)

Received 3 July 2014; Accepted 9 November 2014

Journal of Cell Science (2015) 128, 305–316 doi:10.1242/jcs.158915

membrane-deforming capability that likely contributes to induce or stabilize nuclear membrane curvatures required for pore biogenesis and maintenance (Vollmer et al., 2012). Finally, Rtn1 and Yop1, two endoplasmic reticulum (ER)-bending proteins of the reticulon family that adopt a hairpin-like structure in which hydrophobic segments do not fully span the membrane (Hu et al., 2008) have been shown to induce convex membrane curvature and to contribute to NPC assembly into the intact nuclear envelope in both yeast and vertebrates (Dawson et al., 2009).

We have previously characterized Pom33, a *S. cerevisiae* integral membrane protein that dynamically associates with NPCs as demonstrated using live-cell imaging and immunoelectron microscopy (Chadrin et al., 2010). Pom33 has a paralog in *S. cerevisiae*, Per33, which can associate with NPCs but, unlike Pom33, is mainly localized at the ER and nuclear envelope. Pom33 and Per33 belong to a protein family that has been conserved during evolution. Their unique ortholog in *S. pombe*, Tts1, is also partially enriched at NPCs (Asakawa et al., 2014; Zhang and Oliferenko, 2014), whereas the NPC localization of their human ortholog TMEM33 has not yet been demonstrated. These conserved proteins share two predicted transmembrane domains as well as two long hydrophobic domains. We previously proposed that the latter two domains might adopt a hairpin-like structure and partially insert into membranes as reticulons (Chadrin et al., 2010), although an alternative predicted topology featuring two additional bona fide transmembrane domains was recently proposed for *S. pombe* Tts1 (Zhang and Oliferenko, 2014). *pom33Δ* cells are viable with no detectable transport defect but display an NPC-clustering phenotype (i.e. a non-random distribution of the NPCs along the nuclear envelope), a hallmark of yeast mutants impaired in NPC biogenesis, including Nup84 complex mutants (notably *nup133Δ*) and *rtn1Δ yop1Δ* mutants (Doye and Hurt, 1997; Dawson et al., 2009). In addition, Pom33 physically associates with Rtn1 and becomes crucial for yeast viability in the absence of a functional Nup84 complex or Ndc1 interaction network. The function of Pom33 in NPC biogenesis was further inferred from its synergistic defect in pore assembly upon depletion of Nup170, a Nup previously reported to contribute to NPC assembly (Makio et al., 2009). We previously hypothesized that, by modifying or stabilizing the nuclear-envelope–NPC interface, Pom33 might contribute to efficient assembly and/or stabilization of nuclear pores (Chadrin et al., 2010).

Because of their function in the recruitment of scaffold Nup complexes and/or in membrane curvature induction or stabilization, proper NPC targeting of Poms or membrane-bound Nups is intimately linked to their function in NPC biogenesis. Although the precise mechanisms ensuring proper pore membrane targeting have only been defined for a few Poms, it appears that, as for integral proteins of the INM (reviewed in Katta et al., 2014, Laba et al., 2014), multiple distinct determinants contribute to this process. For instance, the transmembrane domain of vertebrate gp210 has been shown to be sufficient for NPC targeting, but its short C-terminal cytoplasmic tail encompasses an additional sorting determinant (Wozniak and Blobel, 1992). Likewise, proper targeting of vertebrate Pom121, which has a large extraluminal domain, requires NLS sequences that interact with the importin-α–importin-β heterodimer and a nuclear-envelope-targeting sequence that binds to INM proteins (Doucet et al., 2010; Funakoshi et al., 2011).

In this study, we have characterized the NPC-targeting determinants of Pom33. We show that its C-terminal domain (CTD) behaves as an NLS-like Kap123-binding site and encompasses two amphipathic helices. These features are together required for proper localization and function of Pom33 at NPCs.

RESULTS

Pom33 specifically interacts with Kap123

A previous study, based on the affinity purification from yeast cells of a protein-A-tagged version of Pom33 (Pom33–ProtA), identified the reticulon protein Rtn1 as a physical partner of Pom33 (Chadrin et al., 2010). However, Pom33 was still properly localized to the NPCs in *rtn1Δ* cells and even in *rtn1Δ rtn2Δ yop1Δ* cells, in which all yeast reticulon proteins are deleted (supplementary material Fig. S1A), indicating that other determinants are required for Pom33 targeting to NPCs.

To identify additional proteins physically interacting with Pom33, we undertook a mass spectrometry analysis of proteins co-purifying with Pom33–ProtA. We also included samples from wild-type (wt) yeasts and from cells expressing ProtA-tagged Per33, the yeast Pom33 paralog that is mainly localized at the ER and nuclear envelope (Chadrin et al., 2010). Comparing the outcome of two distinct experiments, in which only proteins identified in the Pom33–ProtA but not in the control (wt) sample were considered, led to the identification of the Kap123 nuclear transport factor (supplementary material Table S1). In these two distinct experiments, Kap123 was identified with higher scores in the Pom33–ProtA as compared to Per33–ProtA fractions (supplementary material Table S1), suggesting an enrichment of Kap123 in the Pom33 as compared to the Per33 fractions. The outcome of this qualitative proteomic analysis was validated in independent experiments, by western blot analysis of the affinity-purified fractions using anti-Kap123 antibodies. This analysis confirmed that Kap123 specifically interacts with Pom33 and to a far lower extent with Per33 (Fig. 1A).

We next determined whether Rtn1 could mediate the interaction between Pom33 and Kap123. We therefore performed the Pom33 affinity purification experiment in an *rtn1Δ* context, and found no significant difference in the amount of Kap123 co-purifying with Pom33 in control versus *rtn1Δ* cells (Fig. 1A). Conversely, affinity-purification experiments, performed on Pom33–ProtA cells expressing Rtn1-GFP in a wild-type or *kap123Δ* background, revealed that the interaction between Rtn1 and Pom33 does not require Kap123 (Fig. 1B). Taken together, these data indicate that Pom33 independently interacts with Kap123 and Rtn1.

Kap123 and Kap121 exhibit significant functional redundancy, and several cargoes that are primarily imported by Kap123 use Kap121 as a backup importer (reviewed in Chook and Süel, 2011). However, western blot analysis did not reveal any specific enrichment of Kap121. In addition, only a minor increase was observed for another major importin, Kap95, in the Pom33–ProtA fraction as compared to the control sample (Fig. 1B). In addition, these signals were not enhanced when the affinity purification was performed from *kap123Δ* cell extract, indicating that neither Kap121 nor Kap95 can substitute for Kap123 for Pom33 binding, therefore highlighting the specificity of this interaction.

The CTD of Pom33 is required for its proper targeting to NPCs

We next aimed to determine the region of Pom33 required for its interaction with Kap123. Because Pom33 is an integral membrane protein, we focused our attention on its extraluminal N- and C-terminal domains (Chadrin et al., 2010; see Fig. 2A).

Journal of Cell Science (2015) 128, 305–316 doi:10.1242/jcs.158915

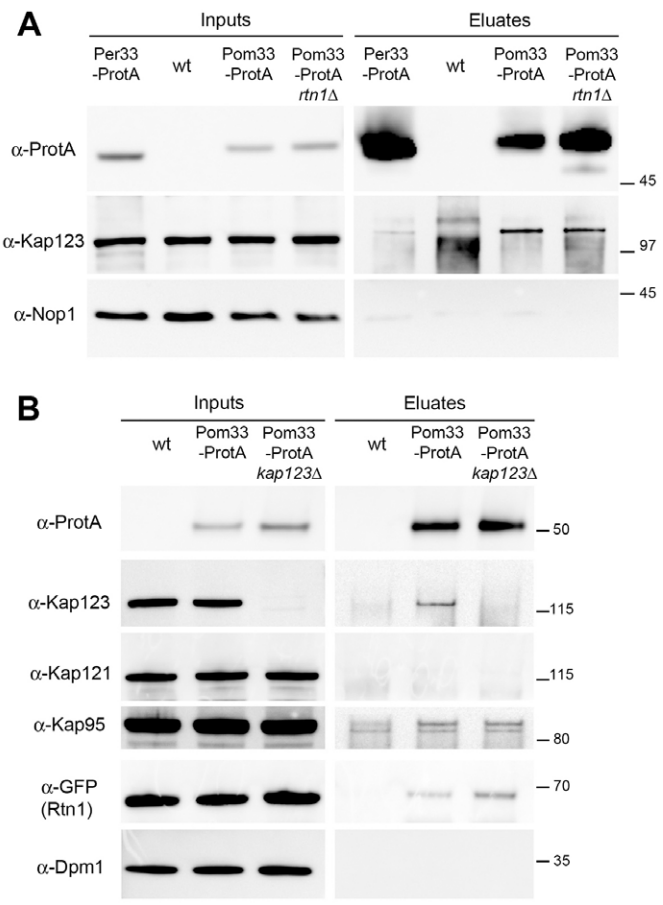

Fig. 1. Pom33 interacts with Kap123. (A) Affinity purification of Per33–ProtA and Pom33–ProtA in wild-type cells and of Pom33–ProtA in *rtn1Δ* cells by IgG chromatography. Wild-type cells (wt), not expressing Pom33–ProtA, were used as control. Total soluble extracts (inputs) and affinity-purified fractions (eluates) were analyzed by western blotting using the indicated antibodies. For the anti-ProtA detection, eluates were diluted 1000 fold. The nucleolar protein Nop1 was used as negative control. Molecular masses are indicated (kDa). (B) Affinity purification of Pom33–ProtA in control or *kap123Δ* cells. All strains used in this panel, including the wild-type cells not expressing ProtA–Pom33 (wt), further express Rtn1–GFP. Samples were analyzed as described in A except that the integral membrane ER protein Dpm1 was used as a negative control.

Therefore, we analyzed the localization and, when achievable, Kap123-binding properties of N- and C-terminally-deleted versions of Pom33, expressed as the unique form of Pom33 in yeast cells. Deletion of the N-terminal domain of Pom33 (amino acids 1–33, see Fig. 2A), affected neither its interaction with Kap123 (supplementary material Fig. S2A) nor its targeting to NPCs (supplementary material Fig. S2B). In contrast, fluorescence analysis of a Pom33–GFP fusion lacking the last 65 amino acids (Pom33$^{\Delta CTD}$–GFP) did not reveal any detectable signal, suggesting that the CTD of Pom33 is required for its stability (our unpublished data). To try to improve the stability of this mutant form of Pom33, we next tagged Pom33$^{\Delta CTD}$–GFP in cells lacking Cue1, a key player in ER-associated degradation (ERAD), a quality control pathway that targets misfolded and misassembled proteins to the ubiquitin-proteasome system (Biederer et al., 1997). Although *CUE1* deletion did not affect the expression or localization of Pom33–GFP (supplementary material Fig. S3), a specific Pom33$^{\Delta CTD}$–GFP fluorescence signal became detectable in *cue1Δ* cells (Fig. 2B). However, unlike Pom33–GFP, Pom33$^{\Delta CTD}$–GFP displayed a smooth staining along the nuclear envelope. Moreover, Pom33$^{\Delta CTD}$–GFP was not significantly enriched within the NPCs that were improperly distributed into clusters along the nuclear envelope in Pom33$^{\Delta CTD}$–GFP-expressing cells (Fig. 2B). This indicates that the Pom33$^{\Delta CTD}$–GFP protein is not properly targeted to the NPCs. Although a direct contribution of Pom33-CTD to NPC distribution cannot be excluded, the NPC-clustering phenotype of *pom33$^{\Delta CTD}$–GFP cue1Δ* cells, which mimics *POM33* inactivation (Chadrin et al., 2010), might reflect the requirement of the CTD for proper localization of Pom33 at NPCs, the place at which this protein would in turn contribute to proper NPC distribution.

The CTD of Pom33 directly interacts with Kap123

To address whether Pom33-CTD interacts directly with Kap123, either GST or distinct GST–Kaps fusion proteins synthesized in *E. coli* were immobilized on glutathione–Sepharose and incubated with recombinant MBP–Pom33-CTD (Fig. 3A). This analysis revealed a reproducible binding of MBP–Pom33-CTD to GST–Kap123 but also to four other importins (Kap114, Kap121, Kap95 and Kap104). In contrast, binding of MBP–Pom33-CTD to importin Kap120 or exportin Cse1 was in the same range as the non-specific binding to GST alone (Fig. 3Aa,b).

Following substrate import into the nucleus, the binding of Ran-GTP to importins contributes to the release of import substrates and prevents their subsequent reassociation with importins (Conti et al., 2006). To determine whether the interaction between Pom33-CTD and this subset of importins is dependent on Ran, recombinant yeast Ran-GTP (Gsp1-Q71L-GTP) was added to GST–Kaps immobilized on glutathione–Sepharose before incubation with MBP–Pom33-CTD. Under these conditions, MBP–Pom33-CTD binding to GST-tagged Kap123, Kap121, Kap95, Kap104 and Kap114 was inhibited, indicating that Pom33-CTD behaves as an NLS (Fig. 3Aa,b). Most of the Kap123 recognition motifs characterized so far are enriched in basic amino acids, although they are more complex and more diverse than classical cNLSs (Fries et al., 2007; Kupke et al., 2011; Chook and Süel, 2011). To determine whether the positively charged residues present within Pom33-CTD contribute to its interaction with Kap123, we mutated the 13 lysine and arginine residues (K and R) within Pom33-CTD to asparagine and glutamine residues (Q and N), respectively (Fig. 3Ba). When used in GST-pulldown experiments, binding of the resulting MBP–Pom33-CTD-KR^{mut} recombinant protein to GST–Kap123 was substantially impaired, pointing to a crucial function of these positively charged amino acids for Pom33-CTD interaction with Kap123 (Fig. 3Bb,c).

To determine the contribution of Kap123–Pom33 interaction to Pom33 targeting and function, we next integrated these 13 K/R to Q/N mutations, along with a GFP tag, at the *POM33* locus. Fluorescence analysis indicated that the NPC targeting of the resulting Pom33-KR^{mut}–GFP protein was not distinguishable from its wild-type counterpart (supplementary material Fig. S1C,D). In addition, unlike in *pom33Δ* (Chadrin et al., 2010) or *pom33$^{\Delta CTD}$–GFP* cells (Fig. 2B), the NPC distribution visualized by Nup49–mCherry was not affected in *pom33-KR^{mut}–GFP* cells (supplementary material Fig. S1D). The lack of detectable phenotype in these cells thus indicates that, within Pom33-CTD, determinants other than its Kap123-binding site contribute to Pom33 targeting to NPCs.

Journal of Cell Science (2015) 128, 305–316 doi:10.1242/jcs.158915

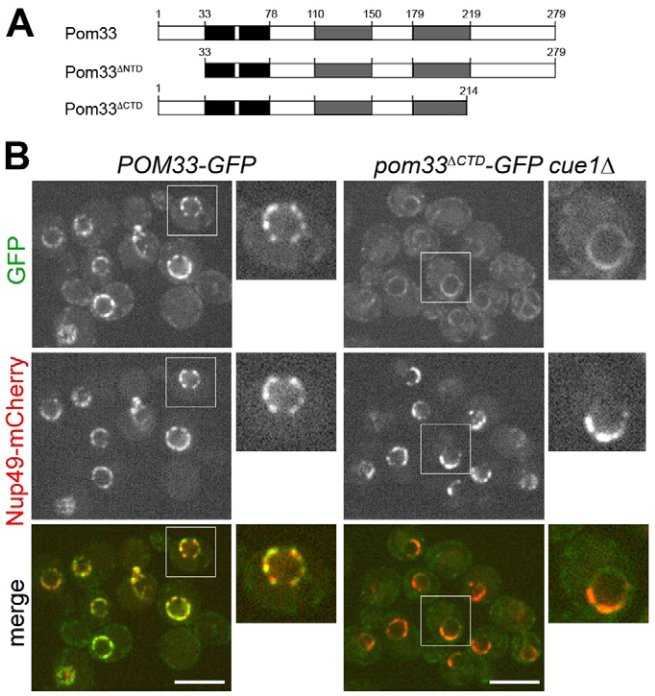

Fig. 2. The C-terminal domain of Pom33 contributes to its targeting to nuclear pores. (A) Schematic organization of Pom33 and the deletion constructs used in this study. The first hydrophobic stretch is predicted with very high reliability to encompass two membrane-spanning segments (black boxes) whereas the two other hydrophobic domains (gray boxes) might adopt a hairpin like structure in which hydrophobic segments do not fully span the membrane (Chadrin et al., 2010). (B) Spinning disk confocal images of *POM33–GFP* and *pom33$^{\Delta CTD}$–GFP cue1Δ* cells grown at 25°C. Both strains further express a plasmid-encoded version of Nup49–mCherry. Twofold enlargements of the marked cells are also presented. Note that Pom33$^{\Delta CTD}$–GFP displays a smoother staining along the nuclear envelope as compared to wild-type Pom33–GFP and is not enriched at the pores (labeled with Nup49–mCherry) that display an altered distribution in *pom33$^{\Delta CTD}$–GFP cue1Δ* cells. Scale bars: 5 µm.

Pom33-CTD encompasses two amphipathic α-helices

It was recently reported that several proteins co-purifying with Kap123 possess putative amphipathic α-helices functioning as in-plane membrane anchors in monotopic membrane proteins, as demonstrated for Nbp1 (Kupke et al., 2011). Likewise, various secondary structure predictions identified two putative α-helices within Pom33-CTD (amino acids 223–240 and 247–263; Fig. 4A; supplementary material Fig. S3A). Moreover, helical wheel representation (generated with HeliQuest; Gautier et al., 2008), revealed the strong amphipathic character of these two α-helices (hereafter named Φ1 and Φ2) (Fig. 4A).

To determine whether these predicted amphipathic helices confer membrane binding to Pom33-CTD, we first used a liposome co-flotation assay. Recombinant MBP–Pom33-CTD was incubated with liposomes [90% (mol/mol) POPC and 10% (mol/mol) DOPS] of various sizes (from ~200 to ~20 nm in diameter; Fig. 4B, supplementary material Fig. S3B), and liposome-bound proteins were separated from unbound proteins by flotation in a discontinuous Nycodenz density gradient. Analysis of liposomes and liposome binding proteins recovered from the top fraction (float) revealed that Pom33-CTD has the capacity to bind to liposomes, with a significantly higher binding efficiency to small (~20 nm in diameter) liposomes (Fig. 4B).

As membrane adsorption of amphipathic helices is coupled to their folding into an α-helix (White et al., 1998), we next used circular dichroism (CD) spectroscopy to determine the secondary structure of Pom33-CTD either in solution or in the presence of liposomes. CD spectra of a Pom33-CTD synthetic peptide were recorded in buffer and in the presence of small POPC:DOPS (90:10) liposomes. Incubation of the peptide with an increasing concentration of liposomes led to a progressive increase in ellipticity at 208 and 222 nm, which is the signature of an α-helical fold (Fig. 4C).

Molar ellipticity at 222 nm was then used to determine the binding free energy of the Pom33-CTD peptide to these liposomes as described previously (Fernández-Vidal et al., 2011) (supplementary material Fig. S4C). The calculated $\Delta G_{binding}$, −6.9 kcal mol^{-1} (−28.9 kJ mol^{-1}), falls in the same range as classical amphipathic helices such as the antimicrobial peptide melittin from bee venom (Fernández-Vidal et al., 2011). This rather high affinity is promoted by three main factors: (1) the presence of two amphipathic helices with both a strong hydrophobic moment and high positive charge within the whole Pom33-CTD peptide, (2) the presence of 10% anionic DOPS lipids, and (3) the high curvature of the liposomes.

The helical content of Pom33-CTD peptide (extracted from the mean residue molar ellipticity at 222 nm as described in Wieprecht et al., 1999; see supplementary material Fig. S4D) reached a maximum of ~45% at 2.5 mM lipids. As the two predicted α-helices (Φ1 and Φ2) represent 31–35 amino acids out of the 65 residues within the Pom33-CTD peptide (48–54% of the total residues; Fig. 4A), this suggests that these two amphipathic helices are almost fully folded into α-helices once bound to liposomes. The CD spectra also revealed a substantial level (~20%) of α-helical content in the absence of lipids (supplementary material Fig. S4D), a property possibly reflecting inter- or intra-molecular protein interactions (see Discussion).

To allow subsequent functional studies of these amphipathic helices without affecting the structure or global charge of Pom33-CTD, we mutated hydrophobic residues in the nonpolar faces of these two helices to asparagine residues (three residues in Φ1 and two in Φ2; Fig. 4Da). Although structure prediction still identified two putative α-helices within the resulting Pom33-CTD-Φ^{mut} sequence (our unpublished data), the mean hydrophobicity <H> and hydrophobic moment <µH> of the two mutated helices were strongly decreased compared to their wild-type counterpart (Fig. 4, compare Fig. 4A to Fig. 4Da). Consistently, when tested in a flotation assay, the recombinant MBP–Pom33-CTD-Φ^{mut} carrying these mutations showed a drastic reduction in liposome association as compared to wild-type MBP–Pom33-CTD (Fig. 4Db). Taken together, these experiments thus validate the existence of two amphipathic helices within Pom33-CTD, which drive binding of this domain to highly curved membranes.

In vivo localization of Pom33-CTD

To investigate the functional implication of the amphipathic helices and Kap123-binding properties of Pom33-CTD, we first expressed plasmid-borne Pom33-CTD (lacking Pom33 transmembrane domains) and its mutant forms fused to GFP in yeast cells. Imaging of Pom33-CTD–GFP revealed a tubular staining within the cytoplasm, strongly reminiscent of a mitochondrial localization, which was confirmed upon co-transformation with a mitochondrial reporter fused to mRFP (Fig. 5A). Although not anticipated, this localization likely reflects the fact that positively charged amphipathic helices are

Journal of Cell Science (2015) 128, 305–316 doi:10.1242/jcs.158915

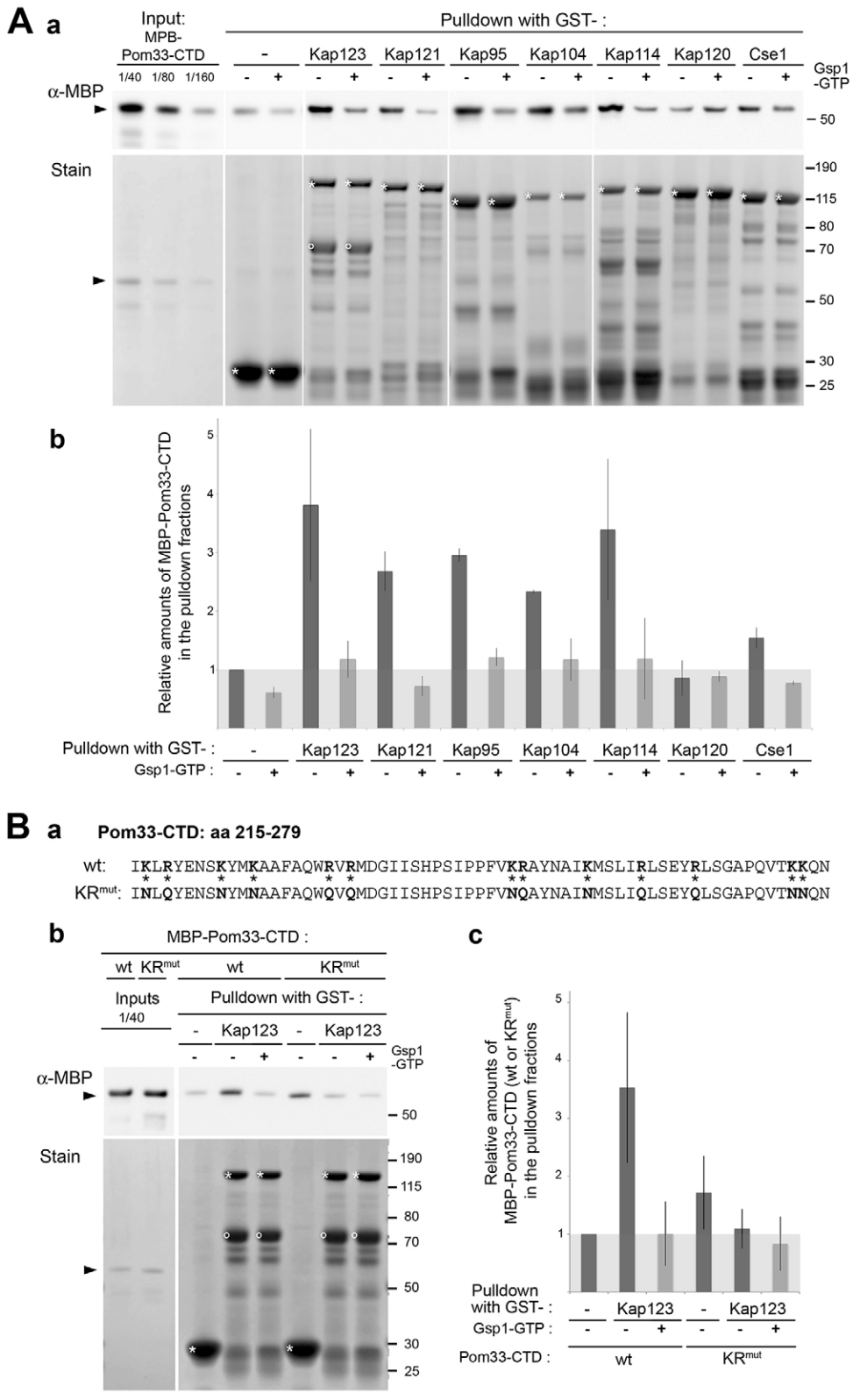

Fig. 3. Pom33-CTD directly interacts *in vitro* with a subset of karyopherins. (A) Equivalent amounts of recombinant GST (−), or of GST-tagged karyopherins (Kap123, Kap121, Kap95, Kap104, Kap114, Kap120 and Cse1) were immobilized on glutathione–Sepharose and incubated with recombinant Gsp1-Q71L-GTP (+) or with buffer alone (−) before incubation with MBP–Pom33-CTD. Serial dilutions of the protein sample used for binding (input) were loaded as indicated. (a) Bound proteins were analyzed by SDS-PAGE followed by western blot with an anti-MBP antibody (top panel, α-MBP) or Coomassie staining (bottom panel, stain). The arrowhead indicates the position of MBP–Pom33-CTD and asterisks mark the positions of the GST fusion proteins. An open circle marks a previously described major degradation product of recombinant GST–Kap123 (Straube et al., 2010). Molecular masses are indicated (kDa). (b) The relative amounts of MBP–Pom33-CTD associated to the various GST-tagged Kaps in the absence (−) or presence (+) of Gsp1-Q71L-GTP were quantified based on serial dilutions of the input. Values (mean±s.d.; $n \geq 2$) were normalized to the input and were further normalized for each independent experiment to the value obtained for GST (background level). (B) (a) Peptide sequence of Pom33 C-terminal domain (Pom33-CTD) used in this study (amino acids 215–279). Stars point to the 13 lysine (K) and arginine (R) residues in the wild-type (wt) sequence that are respectively mutated towards asparagine (N) and glutamine (Q) in the mutagenized form of Pom33-CTD-KR^{mut}. (b) Equivalent amounts of recombinant GST (−), or GST–Kap123, pre-incubated (+) or not (−) with Gsp1-Q71L-GTP, were used for GST pulldown in the presence of recombinant MBP–Pom33-CTD or MBP–Pom33-CTD-KR^{mut} (carrying the 13 K/R to N/Q mutations). (c) Samples were quantified as described in A, b. Note that MBP–Pom33-CTD-KR^{mut}, despite exhibiting a higher non-specific binding to GST alone than MBP–Pom33-CTD, displays an impaired binding to GST–Kap123.

defining features of a subset of mitochondrial-targeting peptides, namely α-helical presequences and internal 'presequence-like' signals (reviewed in Chacinska et al., 2009). Given that full-length Pom33 is anchored into the ER and nuclear envelope through transmembrane domains that are not present within Pom33-CTD–GFP, this mitochondrial localization is unlikely to be physiologically relevant.

Consistent with this hypothesis, the Pom33-CTD-Φ^{mut}–GFP chimera that carries mutations affecting the amphipathic properties of its two α-helices was no longer targeted to the

Journal of Cell Science (2015) 128, 305–316 doi:10.1242/jcs.158915

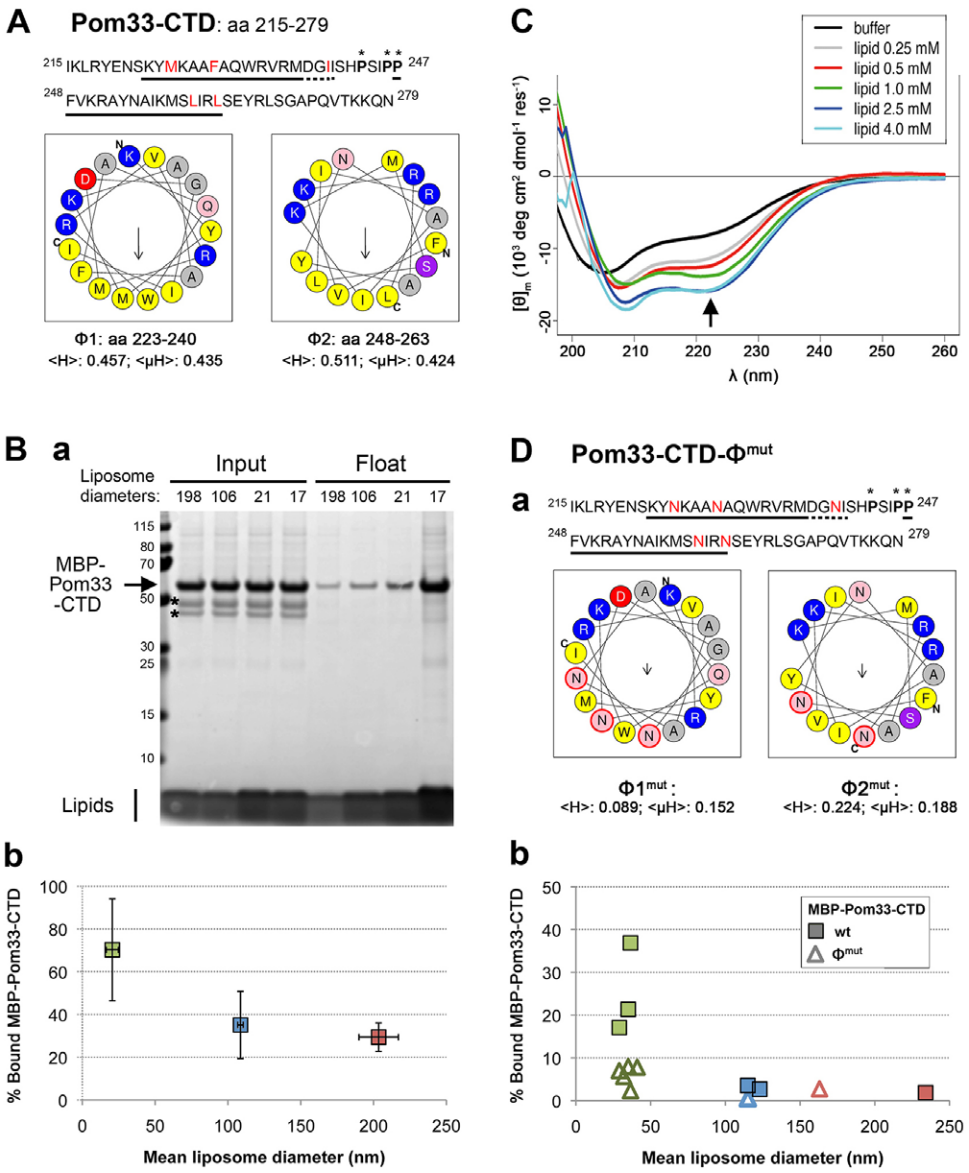

Fig. 4. Two amphipathic helices within Pom33-CTD contribute to its binding to highly curved membranes. (A) Top, amino acid sequence of Pom33-CTD. Underlined are two putative helices Φ1 and Φ2 identified by various secondary structure prediction methods (see supplementary material Fig. S4A). Dotted lines under the Φ1 sequence reflect low prediction confidence. Stars highlight proline residues in-between these two predicted helices. Residues in red are those mutated in D. Bottom, helical wheel representation (generated with HeliQuest; Gautier et al., 2008), illustrating the strong amphipathic character of both Φ1 and Φ2 (for Φ2, the first proline was not included). Yellow, hydrophobic residues; purple, serine; blue, basic residues; red, acidic residues; pink, asparagine and glutamine; gray, other residues. The position of the first (N) and last (C) amino acids of the corresponding peptide sequences are indicated. The length of the arrow is proportional to the mean hydrophobic moment <μH >. For each helix, <μH > and the mean hydrophobicity <H> values (in arbitrary units as returned by HeliQuest) are also indicated. (B) Flotation assay using recombinant MBP–Pom33-CTD protein and liposomes of various sizes. The fractions before (input) and after flotation were analyzed by SDS-PAGE stained with Coomassie. (a) Outcome of a typical experiment. The mean diameter of the liposomes (as determined by DLS, see supplementary material Fig. S4B) used in this experiment is indicated on the top of the gel. The 198 (±80) nm, (mean±s.d.) and 106 (±35) nm liposomes were obtained by extrusion through a polycarbonate membrane of 400 and 100 nm pore size, respectively, and the 21 (±7) and 17 (±4) nm liposomes were generated by tip and bath sonication, respectively. An arrow and a vertical bar indicate the positions of MBP-Pom33-CTD and the lipids, respectively. Molecular masses are indicated (kDa). Note that the two main degradation products of MBP–Pom33-CTD (stars) do not bind to the liposomes. (b) Percentage of MBP–Pom33-CTD binding to liposomes obtained by sonication (green), or extrusion through 100 nm (blue) or 400 nm (red) filters (see Materials and Methods). Error bars in both directions show s.d. from four or five independent experiments using different preparations of recombinant proteins and/or liposomes. (C) Circular dichroism (CD) spectra of the Pom33-CTD synthetic peptide (amino acids 215–279) incubated with various concentrations of small POPC:DOPS (90:10) liposomes (mean diameter ~20 nm). Plotted is the mean residue molar ellipticity ($[\theta]_m$) as a function of wavelength (λ). The arrow points to the 222 nm wavelength used for the determination of free energy of binding and helix fraction of Pom33-CTD (see supplementary material Fig. S4C,D). (D) (a) Top, amino-acid sequence of Pom33-CTD-Φ^{mut}. Mutated residues are highlighted in red. Bottom, helical wheel representation of the two mutagenized sequences ($\Phi1^{mut}$ and $\Phi2^{mut}$). The mutagenized residues are circled in red. (b) Recombinant MBP–Pom33-CTD (wt) and MBP–Pom33-CTD-Φ^{mut} were incubated with liposomes of various sizes as described in B. Each data point represents a different incubation reaction using different preparations of recombinant proteins and/or liposomes. Note that in this new series of experiments the wild-type form of MBP–Pom33-CTD binds less to membranes overall but still much more to highly curved membranes (+20–40%, as in B), a variation that we attribute to the use of a different batch of lipids and/or recombinant proteins.

Journal of Cell Science (2015) 128, 305–316 doi:10.1242/jcs.158915

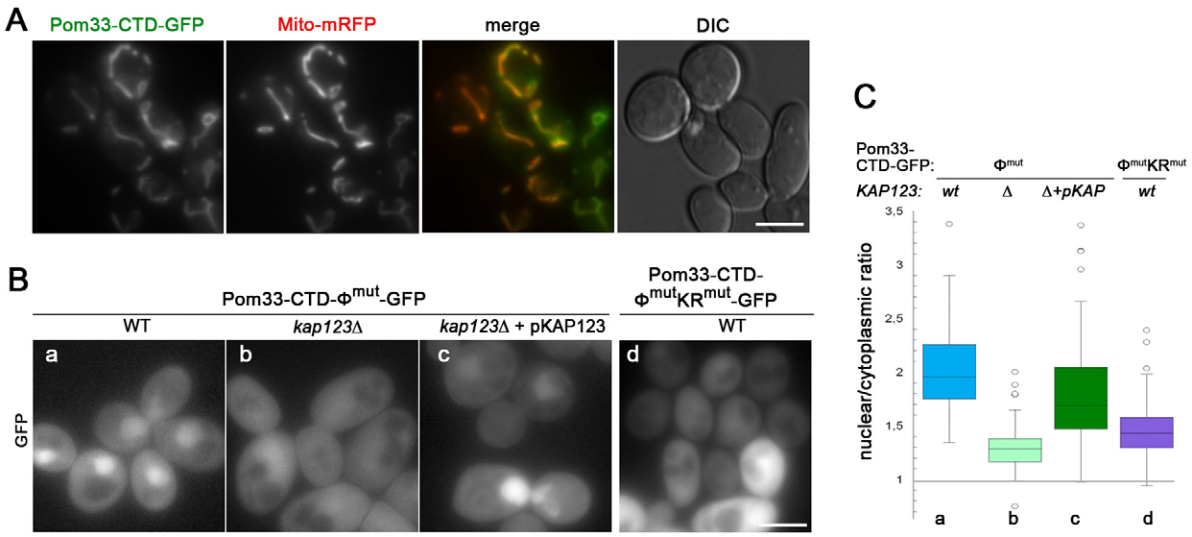

Fig. 5. Pom33-CTD-Φ^{mut}–GFP is imported in the nucleus in a Kap123-dependent manner. (A) Yeast cells carrying centromeric plasmids driving the expression of Pom33-CTD–GFP and of an mRFP-labeled mitochondrial reporter (Mito-mRFP) were analyzed by fluorescence microscopy. Wide-field images of single-channel fluorescence for GFP and mRFP, merge and DIC images are shown. (B) Localization of Pom33-CTD-Φ^{mut}–GFP in wild-type cells (a), *kap123Δ* cells (b) and *kap123Δ* cells carrying a plasmid-borne version of *KAP123* (c), and of Pom33-CTD-Φ^{mut}KR^{mut}–GFP in wild-type cells (d). Wide-field images of single-channel fluorescence for GFP are shown. Scale bars: 5 µm. (C) Images as those presented in Ba–Bd were used to quantify the nuclear:cytoplasmic fluorescence intensity ratio of Pom33-CTD-Φ^{mut}–GFP and Pom33-CTD-Φ^{mut}KR^{mut}–GFP (see Materials and Methods). At least 100 cells were quantified in each condition. Nuclear:cytoplasmic ratios are represented as box plots using KaleidaGraph (Synergy Software). The box represents the 25–75th percentiles, and the median is indicated. The whiskers show the 10–90th percentiles and outliers are indicated.

mitochondria. Instead, this protein was imported into the nucleus when expressed in wild-type yeast cells (Fig. 5Ba). Importantly, Pom33-CTD-Φ^{mut}–GFP relocalized from the nucleus to the cytoplasm in *kap123Δ* cells (Fig. 5Bb) and the nuclear import defect was rescued upon introduction of a wild-type copy of *KAP123* (Fig. 5Bb,c; see also quantifications of nuclear:cytoplasmic ratio in Fig. 5C). These data indicate that *in vivo* Kap123 is the main karyopherin contributing to the nuclear import of the Pom33-CTD-Φ^{mut}–GFP chimera. Consistent with the impaired *in vitro* interaction of Pom33-CTD-KR^{mut} with Kap123 (Fig. 3D), the Pom33-CTD-Φ^{mut}KR^{mut}–GFP chimera, in which mutations of the 13 lysine and arginine residues described above were introduced within Pom33-CTD-Φ^{mut}–GFP, no longer accumulated in the nucleus (Fig. 5Bd,C). Taken together, these data indicate that under conditions abolishing Pom33-CTD membrane association, this domain behaves as a Kap123-dependent NLS.

Combined loss of membrane- and Kap123-binding affects Pom33 localization and function at NPCs

Having established the contribution of the amphipathic helices and charged residues in the context of the truncated Pom33-CTD protein, we next investigated their implication in full-length Pom33 targeting and function. When mutations of the two amphipathic helices were introduced along with a GFP tag at the *POM33* locus, the localization of the resulting Pom33-Φ^{mut}–GFP protein was not distinguishable from its wild-type counterpart, whether expressed in a *NUP133* or a *nup133Δ* background (supplementary material Fig. S1E). In addition, as also observed in the *pom33-KR^{mut}–GFP* mutant, NPC distribution was not affected in *pom33-Φ^{mut}–GFP* cells (supplementary material Fig. S1E). In contrast, a mild NPC-clustering phenotype was observed when these two sets of mutations were combined (*pom33-Φ^{mut}KR^{mut}–GFP* cells; Fig. 6A). In these cells, the Pom33-Φ^{mut}KR^{mut}–GFP protein displayed an increased localization within the ER, and its localization at the nuclear envelope was not restricted to the Nup49–mCherry-labeled NPCs. In *nup133Δ* cells, all the nuclear-envelope-associated Pom33–GFP relocalized in foci coinciding with Nup49–mCherry clusters, whereas Pom33-Φ^{mut}KR^{mut}–GFP was still present outside the NPC clusters. In fact, this localization mimicked the one previously observed for the Pom33 ER-enriched paralog Per33 (Chadrin et al., 2010). Despite this significant mislocalization, Pom33-Φ^{mut}KR^{mut}–GFP still displays a mild accumulation at NPCs, as best seen in *nup133Δ* cells (Figs 6A; supplementary material Fig. S1B). We thus tested whether the previously reported interaction of Pom33 with Rtn1 might underlie this residual NPC targeting of Pom33-Φ^{mut}KR^{mut}–GFP. However, analysis of Pom33-Φ^{mut}KR^{mut}–GFP localization revealed that its minor association with clustered NPCs persists in *rtn1Δ* and *rtn1Δ rtn2Δ yop1Δ* cells (arrows in supplementary material Fig. S1B). This indicates that yet unknown determinants contribute to Pom33 targeting at NPCs.

Analysis of these *pom33-Φ^{mut}KR^{mut}* cells did not reveal any growth defect as compared to wild-type Pom33–GFP-expressing cells (Fig. 6B), an expected result in view of the lack of growth defects in *pom33Δ* cells (Chadrin et al., 2010). In contrast, comparison of the *POM33–GFP nup133Δ* single mutant and *pom33-Φ^{mut}KR^{mut}–GFP nup133Δ* double mutant revealed a synergistic growth defect at 30℃ and 34℃ (Fig. 6B), recapitulating to some extent the genetic interaction previously described between *pom33Δ* and *nup133Δ* (Chadrin et al., 2010).

Taken together, these data thus reveal the contribution of two redundant determinants within Pom33-CTD, namely a pair of amphipathic helices and a Kap123-binding site, for the proper localization of Pom33. These two determinants appear in turn to be required for Pom33 function at NPCs.

Journal of Cell Science (2015) 128, 305–316 doi:10.1242/jcs.158915

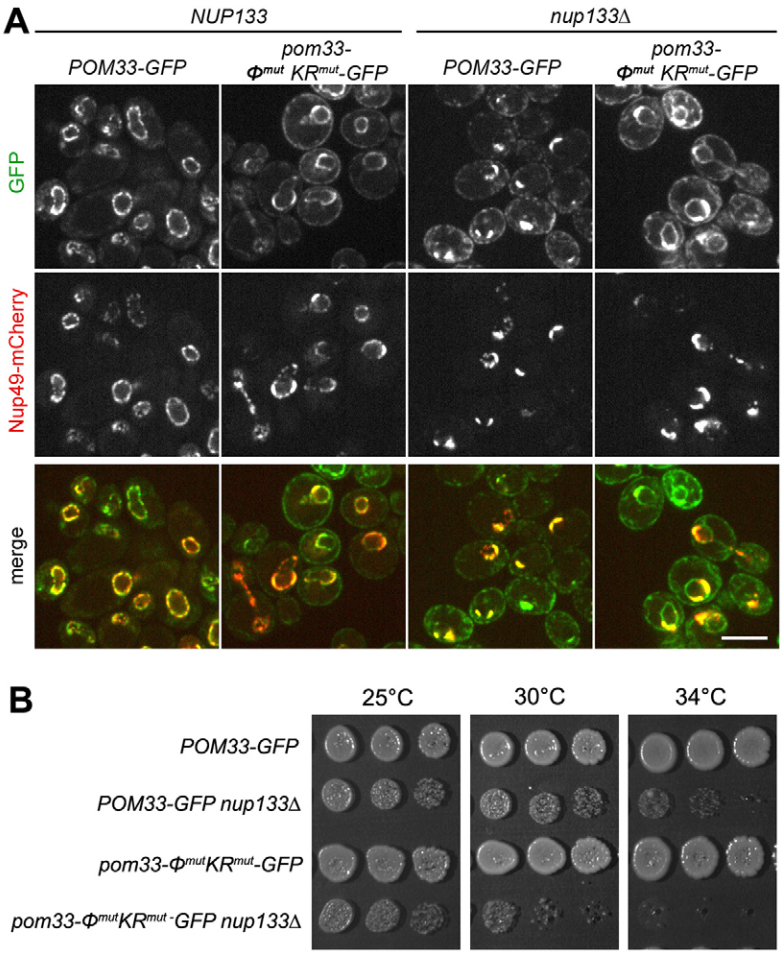

Fig. 6. Combined mutations of amphipathic helices and charged residues within Pom33-CTD affect Pom33 localization and lead to a genetic interaction with *nup133Δ*. (A) Spinning disk confocal images of Pom33–GFP and Pom33-$\Phi^{mut}KR^{mut}$–GFP expressing cells in wild-type *NUP133* and *nup133Δ* contexts. All strains further express a plasmid-encoded version of Nup49–mCherry and were grown at 25˚C. Note that unlike Pom33–GFP, localization of Pom33-$\Phi^{mut}KR^{mut}$–GFP is not restricted to the nuclear pores (labeled with Nup49–mCherry). Scale bar: 5 µm. (B) Growth properties of *POM33–GFP* and *pom33-$\Phi^{mut}KR^{mut}$–GFP* cells in a wild-type and *nup133Δ* background. Equivalent amounts of cells were spotted as fivefold dilutions (left to right) on YEPD plates, and plates were incubated for 3 days at 25, 30 and 34˚C.

DISCUSSION

In this study, we have identified Kap123 as a new binding partner of the nucleoporin Pom33. Although most interactions between Nups and Kaps involve FG-repeat containing domains (Terry and Wente, 2009), the Pom33 protein sequence does not include any FG repeats. In addition, the nuclear import of a typical Kap123 substrate (Rpl25-NLS–GFP, Timney et al., 2006) is not significantly altered in *pom33Δ* cells (our unpublished data). In contrast, our data indicate that, as previously reported for a few Nups (yeast Nup53 and Nic96 and vertebrate Nup153, Nup98 and Tpr; Lusk et al., 2002 and references therein), the CTD of Pom33 contains a Kap-dependent NLS-like domain because: (1) Pom33-CTD directly interacts *in vitro* with Kap123, and lysine and arginine (KR) residues within Pom33-CTD contribute to this interaction (Fig. 3), (2) Pom33-CTD–Kap123 association is impaired in the presence of Ran-GTP, a hallmark of NLS–importin interactions (Fig. 3); and (3) the Pom33-CTD-Φ^{mut}–GFP fusion protein, in which Pom33-CTD cytoplasmic retention is abolished, is imported into the nucleus in a Kap123- and KR-residue-dependent manner (Fig. 5). *In vitro*, recombinant Pom33-CTD was also found to bind to several other importins, notably those previously reported to interact with H2B and Asr1 (Fries et al., 2007; Fig. 3A). However, nuclear import of Pom33-CTD-Φ^{mut}–GFP was fully inhibited in *kap123Δ* cells (Fig. 5B,C), indicating that Kap123 is the main karyopherin contributing *in vivo* to the NLS-mediated nuclear import of Pom33-CTD. Consistent with this result, no other importin was found to efficiently co-purify with Pom33-ProtA, even in *kap123Δ* cells (Fig. 1B).

Although our *in vitro* and *in vivo* data indicate that nuclear accumulation of Pom33-CTD-Φ^{mut}–GFP could be driven by the Ran-GTP-dependent release of Kap123 in the nucleus (Fig 3; Fig. 5B,C), the interaction between endogenous Pom33 and Kap123 is unlikely to be dissociated by Ran-GTP. Indeed, NLS-driven translocation of integral membrane proteins through the nuclear pore membrane has been shown to require a long (at least 120 residues) disordered linker that permits the translocation of NLS-bound karyopherins through the central channel of the NPC (Meinema et al., 2011). Based on predicted topologies (Chadrin et al., 2010; Fig. 2A; Zhang and Oliferenko, 2014), the Pom33 extraluminal CTD is unlikely to fulfill this criterion. If relevant, Pom33 movement across the pore membrane thus likely takes place through the peripheral NPC channels, whose small size cannot accommodate Kap123 (Maimon et al., 2012). As a component of the pore membrane, Pom33 might even not have to translocate to the INM but could facilitate pore formation from the ONM. We thus propose that Kap123 might facilitate the targeting of Pom33 from the ER to the cytosolic side of the NPCs, where a Ran-independent process would drive dissociation of the Pom33–Kap123 complex. This process could involve competition with yet uncharacterized Pom33-CTD-binding partners, as previously described for the Nup53–Kap121 interaction that is inhibited by competing binding to Nup170 (Lusk et al., 2002; Makhnevych et al., 2003).

The fact that Kap123 interacts to a far lower extent with Per33 as compared to Pom33 (Fig. 1A) and that Per33–GFP is less

Journal of Cell Science (2015) 128, 305–316 doi:10.1242/jcs.158915

enriched at NPCs as compared to Pom33 (Chadrin et al., 2010) suggests that interaction with Kap123 might contribute to the improved NPC targeting of Pom33 as compared to Per33. However, Pom33-KR^{mut}–GFP is still properly targeted to NPCs (supplementary material Fig. S1B), indicating that determinants other than Kap123 binding are required for Pom33 localization at NPCs.

Our study further demonstrated the presence of two short amphipathic helices within Pom33-CTD that contribute to its binding to lipid membranes, with a preference for highly curved sonicated liposomes as compared to larger extruded liposomes (Fig. 4). To date, several distinct types of amphipathic helices have been reported to bind preferentially to highly curved membranes. ALPS motifs have a well-developed hydrophobic face, but very few charged residues on their polar face (Drin et al., 2007), whereas the amphipathic helices of α-synuclein and to some extent of Atg3 feature a restrained hydrophobic face and the presence of some charged residues at the interface between the polar and hydrophobic faces (Pranke et al., 2011; Nath et al., 2014). In contrast, both amphipathic helices within Pom33-CTD resemble classic lipid-binding amphipathic helices, with a high hydrophobic moment (>0.42) owing to large hydrophobic residues on the apolar face and some positively charged residues predicted to be positioned at the water–lipid interface (Fig. 4A). These properties probably contribute to the high affinity of Pom33-CTD for lipids in our CD experiments (Fig. 4C). Another major difference between the Pom33-CTD amphipathic helices and curvature sensors described to date (for example, ALPS motifs or α-synuclein) is the presence of helical structures in Pom33-CTD in the absence of lipids. This partial folding in solution might be stabilized by intermolecular interactions between distinct peptides or might reflect intra-molecular interactions, as for instance reported for the N-terminal amphipathic helix of Arf1 (Liu et al., 2010). In the case of Pom33-CTD, the Φ1 and Φ2 α-helices might fold onto each other in the absence of membranes, an hypothesis consistent with some models generated using HHpred (Söding et al., 2005), which predict an α-hairpin between these two helices in solution (our unpublished data). These inter- or intra-molecular interactions between the amphipathic helices of Pom33-CTD could be competing for lipid binding, and perhaps contribute to its curvature-sensing properties. The diversity in the types of amphipathic helices and in the mechanisms allowing them to preferentially bind to curved membranes likely reflects their specificity for distinct membrane-bound compartments as well as their multiple cellular functions.

Some lipid-binding amphipathic helices also interact with proteins, as demonstrated for the synaptobrevin2 SNARE domain (Ellena et al., 2009; Liang et al., 2014) or the N-terminal mitochondrial presequences that interact with a hydrophobic groove on the Tom20 receptor (reviewed in Chacinska et al., 2009). Unlike Pom33-CTD, which appears to be improperly recognized by this mitochondrial translocation machinery (Fig. 5A), endogenous Pom33 is anchored in the ER and nuclear envelope through its N-terminal transmembrane domains, and is therefore unlikely to interact with Tom20. Although Pom33-CTD amphipathic helices could possibly bind to the hydrophobic domain of other proteins, a membrane-curvature-sensing function of this domain appears more likely in view of Pom33 localization at NPCs. Indeed, size measurement of the sonicated liposomes used in this study revealed that most of them have a diameter of ∼20–30 nm (Fig. 4B,Db). As this size is comparable to the distance between the INM and ONM (∼30 nm; West et al., 2011), it is tempting to speculate that by sensing the curved topology of the pore membrane, these amphipathic helices could facilitate the targeting of Pom33 to the NPC. However, binding to curved membranes is neither necessary nor sufficient to ensure efficient association of Pom33 to NPCs (supplementary material Fig. S1B).

Our data further indicate that mislocalization of Pom33 only occurs when both Kap123 and lipid binding are simultaneously impaired (Fig. 6A; supplementary material Fig. S1C–E). The combination of a Kap121- or Kap123-dependent NLS with an amphipathic helix was previously reported for yeast Nup53 and the spindle pole body (SPB) component Nbp1 (Marelli et al., 2001; Patel and Rexach, 2008; Kupke et al., 2011; Vollmer et al., 2012). Unlike the Pom33–Kap123 interaction, the NLSs of Nup53 and Nbp1 were shown to be essential in themselves for their intranuclear targeting. In the case of Nbp1, it has been further proposed that Kap123 binding would shield the amphipathic helix until the protein reaches the nucleus, where its amphipathic helix could act to rearrange and/or stabilize the inner nuclear membrane, thereby contributing to SPB biogenesis (Kupke et al., 2011). However, unlike these two proteins, Pom33 interaction with the nuclear membrane does not solely rely on its amphipathic helices as its primary sequence also includes two membrane-spanning segments and two hydrophobic domains (Fig. 2A). Although an additional membrane-remodeling activity of Pom33 amphipathic helices cannot be excluded, our data rather point to a coordinated function of Kap123 and lipid binding in the targeting of Pom33 to the curved pore membrane. Noteworthy, Pom33 amphipathic helices appear to be conserved during evolution. Indeed, we identified two predicted amphipathic helices in both *S. cerevisae* Per33 and mammalian TMEM33 C-terminal domains (our unpublished results). In addition, while this manuscript was under revision, mutations within a predicted amphipathic helix within *S. pombe* Tts1 (corresponding to the Pom33 Φ2 amphipathic helix) were reported to affect ER shaping and mitotic NPC distribution, although their impact on Tts1 targeting to NPCs was not determined (Zhang and Oliferenko, 2014),

Analyses of the *pom33-Φ^{mut}KR^{mut}–GFP* mutant revealed a genetic interaction with *nup133Δ* and a mild alteration of NPC distribution (Fig. 6) that might, as previously discussed (Chadrin et al., 2010), underscore the contribution of Pom33 to efficient NPC assembly. However, the NPC clustering phenotype of these mutant cells is not as pronounced as in *pom33Δ* or *pom33^{ΔCTD}–GFP* mutants, likely reflecting the fact that the resulting Pom33-Φ^{mut}KR^{mut}–GFP protein still displays a mild accumulation at NPCs, even in the absence of its other previously characterized partner, Rtn1 (supplementary material Fig. S1E). These data indicate that, as previously documented for several inner nuclear membrane proteins (Katta et al., 2014; Laba et al., 2014), redundant mechanisms and/or signals are required for proper NPC targeting of Pom33. In the future, additional studies will be required to understand how the two new Pom33 features described in this study cooperate with other factors to ensure proper NPC assembly and function.

MATERIALS AND METHODS

Yeast strains and plasmids

The strains used in this study are listed in supplementary material Table S2 and are all isogenic to S288C. Yeast cells were grown in standard yeast extract peptone dextrose (YPD) or synthetic complete (SC) medium lacking appropriate amino acids. Unless indicated, cells were grown at 30°C. Transformation, mating and sporulation were performed as

previously described (Chadrin et al., 2010). Construction of plasmids (detailed in supplementary material Table S3) was performed using standard molecular cloning techniques.

Purification of Pom33- and Per33 ProtA-tagged proteins and mass spectrometry analysis

ProtA-tagged versions of Pom33 or Per33 were affinity purified from whole-cell lysates using IgG-conjugated magnetic beads as described previously (Bretes et al., 2014), except that an additional washing step with extraction buffer supplemented with 150 mM NaCl and 1 mg/ml heparin was introduced before elution as reported previously (Alber et al., 2007). Lyophilized eluates were resuspended either in SDS sample buffer for SDS-PAGE or in 25 mM ammonium carbonate for mass spectrometry.

Mass spectrometry analysis was performed essentially as described previously (Bretes et al., 2014). Tryptic digests were analyzed on a LTQ Velos Orbitrap (Thermo Fisher Scientific, San Jose, CA) coupled to an Easy nano-LC Proxeon system (Thermo Fisher Scientific, San Jose, CA). Data were processed with Proteome Discoverer 1.2.0.207 software (Thermo Fisher Scientific, San Jose, CA) coupled to an in-house Mascot search server (Matrix Science, Boston, MA; version 2.4.1). The mass tolerance of fragment ions was set to 10 ppm for precursor ions and 0.6 Da for fragments.

Expression, purification and binding of recombinant proteins

MBP and GST fusion proteins were expressed in Rosetta (DE3) *E. coli* cells transformed with the appropriate plasmids and grown in LB medium (containing 5 g/l NaCl and 2 g/l glucose in the case of MBP fusion production). Expression of the recombinant proteins was induced with 1 mM isopropyl-β-D-thiogalactopyranoside at 37℃ for 2 h (25℃ for 3 h in the case of GST–Kap120 induction). Bacterial pellets were resuspended either in MBP buffer (20 mM Tris-HCl pH 7.5, 200 mM NaCl, 1 mM EDTA, 1 mM DTT and 10% glycerol) or GST buffer (20 mM Hepes, pH 7.5, 110 mM potassium acetate, 2 mM $MgCl_2$, 0.1% Tween 20, 15% glycerol and 1 mM DTT), frozen in liquid nitrogen, thawed and lysed by sonication. The cell lysates were cleared by centrifugation at 10,000 ***g*** for 20 min at 4℃ and soluble fractions were directly used either for GST pull-downs (see below), or for purification of MBP fusion proteins on amylose resin (New England Biolabs) according to the manufacturer's instructions. MBP fusion proteins were eluted in MBP buffer supplemented with 10 mM maltose and kept at 4℃ for short-term use. GTP-bound 6His-tagged Gsp1 was prepared as previously described (Maurer et al., 2001).

GST-pulldown assays were performed essentially as described previously (Straube et al., 2010). Briefly, soluble bacterial extracts containing GST or GST–Kaps were bound to 50 µl of glutathione–Sepharose 4B resin (GE Healthcare) for 1 h at 4℃. The beads were washed three times with GST buffer and blocked with 1 ml of GST buffer containing 1% BSA for 1 h at 4℃. When indicated, beads were further incubated with 30 µM of 6His–Gsp1-Q71L-GTP in GST buffer containing 1% BSA for 1 h at 4℃. Prebound GST or GST–Kaps were incubated with recombinant MBP–Pom33-CTD fusions for 90 min at 4℃. Typical binding reactions involved 500 nM of GST or GST–Kaps and 2–6 µM of MBP fusions. Beads were then washed three times with GST buffer, three times with GST buffer supplemented with 440 mM potassium acetate, and once with GST buffer. Bound proteins were eluted with SDS sample buffer.

Protein analysis

Protein samples were separated on 10% or 4–12% SDS-PAGE gels and stained with Coomassie or transferred onto nitrocellulose filters. Staining was performed using Page Blue Protein Staining Solution (Thermo Scientific), an alcohol-free reagent that does not solubilize the lipids from the gel (Boucrot et al., 2012). Blots were saturated with Tris-buffered saline (TBS), 0.1% Tween 20 and 5% dried milk. For analyses of fractions purified by IgG chromatography, 10% human serum was added at the blocking stage, except for ProtA detection. The resulting blots were probed with the following antibodies: horseradish peroxidase (HRP)-conjugated rabbit anti-HRP polyclonal antibody (1:5000; rabbit PAP; Dakocytomation), anti-GFP (1:500; monoclonal clones 7.1/13.1; Roche), rabbit polyclonal anti-Kap123 (1:5000), Kap121 (1:2000), or Kap95 (1:1000) antibodies (Patel and Rexach, 2008); anti-Nop1 (1:200; monoclonal A66; Tollervey et al., 1991); anti-Dpm1 (1:2000; monoclonal 5C5; Invitrogen); or anti-MBP (1:5000; monoclonal, HRP-conjugated; New England Biolabs). Primary antibodies were detected with HRP-coupled anti-mouse-IgG + IgM or anti-rabbit-IgG secondary antibodies (Jackson ImmunoResearch) and enhanced chemiluminescence followed by detection using a FujiFilm LAS4000 imager. Quantification of signals was performed based on serial dilutions of reference samples using the ImageJ software.

Fluorescence microscopy on yeast cells

Yeast live-cell imaging was performed using exponentially growing cultures. For localization of Pom33–GFP (or its mutant forms) and Nup49–mCherry, fluorescence images were acquired using a spinning disk confocal head (CSU-X1; Yokogawa Corporation of America) mounted on a Ti-E inverted microscope (Nikon) equipped with 491 and 561 nm lasers (Roper Scientific), both using a triple band filter (515–535 nm, 590–615 nm and 690–730 nm), and a charge-coupled device (CCD) camera (Coolsnap HQ2; Photometrics).

For localization of Pom33-CTD–GFP chimera, direct epifluorescence images and differential interference contrast (DIC) images were acquired using a LEICA DM6000B microscope with a 100×, NA 1.4 (HCX PL APO) oil immersion objective and a CCD camera (CoolSNAP HQ; Photometrics). Images were scaled equivalently using Metamorph 5 (Universal Imaging) and processed with Adobe Photoshop CS 8.0 software. Quantifications of the nuclear:cytoplasmic (N:C) ratio were performed using MetaMorph software. Total fluorescence intensities within circular regions of 10 pixels placed in the nuclei (identified, if required, using the Nup49–mCherry signal), in the cytoplasm, and in the intercellular background were measured. N:C ratios were calculated as N:C=(Nucleus–background)/(Cytoplasm–background). Box-plots were generated using Kaleidagraph as previously detailed (Chadrin et al., 2010).

Liposomes reconstitution

The lipids used in this study – 1-palmitoyl-2-oleoyl-sn-glycero-3-phosphocholine (POPC) and 1,2-dioleoyl-sn-glycero-3-phospho-L-serine (DOPS) – were purchased from Avanti Polar Lipids as chloroform solutions. Liposomes used in the co-flotation assay were formed by the extrusion or sonication methods. In both methods, 1 µmol of a lipid mixture (in chloroform) consisting of 90% (mol/mol) POPC and 10% (mol/mol) DOPS was dried in a glass tube for 10 min under a gentle stream of argon and for 1 h under vacuum. The dried lipid film was resuspended in 1 ml of MBP buffer without EDTA and DTT by vigorously vortexing for 1 h at room temperature. The resulting multilamellar liposome suspension was frozen in liquid nitrogen for 30 s and thawed in a 37℃ water bath for 2 min; this cycle was repeated seven times. In the extrusion method, the liposomes were forced at least 21 times through a polycarbonate membrane with a 400 or 100 nm pore size, using the Mini-Extruder from Avanti. In the sonication method, the liposomes were disrupted using either (1) a tip sonicator for ~30 min on ice (Vibra-Cell from Sonics equipped with a 2 mm microtip) through cycles of 30 s on at 20% effective power and 30 s off, or (2) a bath sonicator (Avanti) for ~1 h at room temperature until the solution appeared clear. Metal particles and large liposomes in the tip-sonicated samples were removed by centrifugation for 20 min at 200,000 ***g***. Liposomes used in the CD assay were formed at 12 mM in 5 mM Na_2HPO_4/NaH_2PO_4, pH 7.5, using the bath sonication method as described above. Liposome preparations were kept at 4℃ for up to 1 week.

Liposome size characterization

Liposome size was measured before each experiment by dynamic light scattering (DLS) using the Zetasizer Nano ZS (Malvern Instruments) with liposomes diluted at 100 µM final in MBP buffer without EDTA

and DTT. The obtained intensity distributions were converted into number distributions using the coated-sphere transformation method (provided by the Zetasizer Research software) with the following parameters: particle core refractive index=1.33, shell refractive index=1.43, and core radius-to-shell ratio=20, 10 and 5 for 400 nm extruded, 100 nm extruded and sonicated liposomes, respectively (see supplementary material Fig. S4B).

Liposome co-flotation assay

To assess membrane binding of purified proteins, equal volumes (~100 µl) of recombinant proteins (~10 µM) and liposomes of various sizes (~1 mM) were mixed together at a lipid-to-protein molar ratio of 100 for 2 h at room temperature under intermittent gentle mixing (1 min at 300 rpm every 15 min). 50 µl was taken out to serve as input control and the remaining 150 µl was mixed with 150 µl of 80% (w/v) Nycodenz in MBP buffer without EDTA and DTT. The mixtures were transferred to centrifuge tubes (Ultra-Clear 5×41 mm, Beckman) and overlaid with 250 µl of 30% (w/v) Nycodenz in the same buffer followed by 50 µL of buffer alone. The resulting gradients were centrifuged at 192,000 ***g*** for 4 h at 4℃ in a SW55-Ti rotor (Beckman). 50 µl of liposomes was collected from the top layer (floated fraction), mixed with 4×SDS sample buffer and analyzed by SDS-PAGE stained with Coomassie as described above. Images were acquired using a Gel Doc EZ system (Bio-Rad). Lipid and protein amounts in the input and floated fractions were determined with the Metamorph software. The percentage of liposome-bound proteins was determined by using the content of the inputs as references. Values were further normalized to the percentage of recovered lipids.

Circular dichroism

Pom33-CTD synthetic peptide was purchased from ProteoGenix (purity >98%). CD spectra were recorded on a Jasco J-815 spectrometer over the wavelength range 190–260 nm using a 0.1 cm path length quartz cell. The temperature was set to 25℃ and the scan speed to 10 nm/min at 0.2 nm intervals. The final spectra were averaged over five scans. For each spectrum, we used a peptide concentration of 25 µM in 5 mM Na_2HPO_4/NaH_2PO_4, pH 7.5, without or with 0.25 to 4.0 mM sonicated liposomes. Control spectra of buffer with or without liposomes were systematically subtracted from the spectra with peptides.

Acknowledgements

We are grateful to L. Khemtemourian (Université Pierre et Marie Curie, CNRS, UMR 7203, Paris) for assistance on Circular Dichroism, to F. Carn (Université Paris Diderot) and the French Labex SEAM (Sciences and Engineering for Advanced Materials and devices) supported by CGI (Commissariat Général à l'Investissement) for granting access to the DLS device, to L. Hentges, W. Prinz, M. Rexach, M. Rout, E. Schiebel and J. Shaw for reagents, to M. Garcia and F. Devaux (LCQB, Université Pierre et Marie Curie, Paris) for advices with mitochondrial targeting, to J. Dumont (IJM, Paris) for help with spinning disk imaging, to the IJM Proteomics facility and to C. Jackson (IJM, Paris) for helpful discussion and critical reading of the manuscript.

Competing interests

The authors declare no competing interests.

Author contributions

A.G.F., D.T., P.F.J.F., B.P. and V.D. designed the project. A.G.F., D.T., P.F.J.F., A.C., I.N., T.L., G.S., B.P. and V.D. performed the experiments and analyzed the data. A.G.F., D.T., P.F.J.F., B.P. and V.D. wrote the manuscript.

Funding

These studies were supported by the Centre national de la recherche scientifique (CNRS); by the Fondation ARC pour la Recherche sur le Cancer ['Programme ARC' to V.D and 6 months fellowship to A.C.]; by the 'Who am I?' laboratory of excellence [grant numbers ANR-11-LABX-0071, ANR-11-IDEX-0005-01, contributing to 6 months fellowship to A.G.F.]; by the ANR Jeunes Chercheurs [grant number ANR-09-JCJC-0062-01 to D.T.]; by the AFM Trampoline [grant number 16799 to D.T.]; by the Deutsche Forschungsgemeinschaft and the Homburger Forschungsförderung (to G.S.); and by the Ministère de l'Enseignement Supérieur et de la Recherche (PhD fellowships to A.G.F and A.C).

Supplementary material

Supplementary material available online at
http://jcs.biologists.org/lookup/suppl/doi:10.1242/jcs.158915/-/DC1

References

Aitchison, J. D. and Rout, M. P. (2012). The yeast nuclear pore complex and transport through it. *Genetics* **190**, 855-883.
Alber, F., Dokudovskaya, S., Veenhoff, L. M., Zhang, W., Kipper, J., Devos, D., Suprapto, A., Karni-Schmidt, O., Williams, R., Chait, B. T. et al. (2007). The molecular architecture of the nuclear pore complex. *Nature* **450**, 695-701.
Asakawa, H., Yang, H. J., Yamamoto, T. G., Ohtsuki, C., Chikashige, Y., Sakata-Sogawa, K., Tokunaga, M., Iwamoto, M., Hiraoka, Y. and Haraguchi, T. (2014). Characterization of nuclear pore complex components in fission yeast Schizosaccharomyces pombe. *Nucleus* **5**, 149-162.
Biederer, T., Volkwein, C. and Sommer, T. (1997). Role of Cue1p in ubiquitination and degradation at the ER surface. *Science* **278**, 1806-1809.
Boucrot, E., Pick, A., Çamdere, G., Liska, N., Evergren, E., McMahon, H. T. and Kozlov, M. M. (2012). Membrane fission is promoted by insertion of amphipathic helices and is restricted by crescent BAR domains. *Cell* **149**, 124-136.
Bretes, H., Rouviere, J. O., Leger, T., Oeffinger, M., Devaux, F., Doye, V. and Palancade, B. (2014). Sumoylation of the THO complex regulates the biogenesis of a subset of mRNPs. *Nucleic Acids Res.* **42**, 5043-5058.
Chacinska, A., Koehler, C. M., Milenkovic, D., Lithgow, T. and Pfanner, N. (2009). Importing mitochondrial proteins: machineries and mechanisms. *Cell* **138**, 628-644.
Chadrin, A., Hess, B., San Roman, M., Gatti, X., Lombard, B., Loew, D., Barral, Y., Palancade, B. and Doye, V. (2010). Pom33, a novel transmembrane nucleoporin required for proper nuclear pore complex distribution. *J. Cell Biol.* **189**, 795-811.
Chook, Y. M. and Süel, K. E. (2011). Nuclear import by karyopherin-βs: recognition and inhibition. *Biochim. Biophys. Acta* **1813**, 1593-1606.
Conti, E., Müller, C. W. and Stewart, M. (2006). Karyopherin flexibility in nucleocytoplasmic transport. *Curr. Opin. Struct. Biol.* **16**, 237-244.
Dawson, T. R., Lazarus, M. D., Hetzer, M. W. and Wente, S. R. (2009). ER membrane-bending proteins are necessary for de novo nuclear pore formation. *J. Cell Biol.* **184**, 659-675.
Doucet, C. M., Talamas, J. A. and Hetzer, M. W. (2010). Cell cycle-dependent differences in nuclear pore complex assembly in metazoa. *Cell* **141**, 1030-1041.
Doye, V. and Hurt, E. (1997). From nucleoporins to nuclear pore complexes. *Curr. Opin. Cell Biol.* **9**, 401-411.
Drin, G., Casella, J. F., Gautier, R., Boehmer, T., Schwartz, T. U. and Antonny, B. (2007). A general amphipathic α-helical motif for sensing membrane curvature. *Nat. Struct. Mol. Biol.* **14**, 138-146.
Ellena, J. F., Liang, B., Wiktor, M., Stein, A., Cafiso, D. S., Jahn, R. and Tamm, L. K. (2009). Dynamic structure of lipid-bound synaptobrevin suggests a nucleation-propagation mechanism for trans-SNARE complex formation. *Proc. Natl. Acad. Sci. USA* **106**, 20306-20311.
Fernández-Vidal, M., White, S. H. and Ladokhin, A. S. (2011). Membrane partitioning: ''classical'' and ''nonclassical'' hydrophobic effects. *J. Membr. Biol.* **239**, 5-14.
Floch, A. G., Palancade, B. and Doye, V. (2014). Fifty years of nuclear pores and nucleocytoplasmic transport studies: multiple tools revealing complex rules. *Methods Cell Biol.* **122**, 1-40.
Fries, T., Betz, C., Sohn, K., Caesar, S., Schlenstedt, G. and Bailer, S. M. (2007). A novel conserved nuclear localization signal is recognized by a group of yeast importins. *J. Biol. Chem.* **282**, 19292-19301.
Funakoshi, T., Clever, M., Watanabe, A. and Imamoto, N. (2011). Localization of Pom121 to the inner nuclear membrane is required for an early step of interphase nuclear pore complex assembly. *Mol. Biol. Cell* **22**, 1058-1069.
Gautier, R., Douguet, D., Antonny, B. and Drin, G. (2008). HELIQUEST: a web server to screen sequences with specific α-helical properties. *Bioinformatics* **24**, 2101-2102.
Hu, J., Shibata, Y., Voss, C., Shemesh, T., Li, Z., Coughlin, M., Kozlov, M. M., Rapoport, T. A. and Prinz, W. A. (2008). Membrane proteins of the endoplasmic reticulum induce high-curvature tubules. *Science* **319**, 1247-1250.
Katta, S. S., Smoyer, C. J. and Jaspersen, S. L. (2014). Destination: inner nuclear membrane. *Trends Cell Biol.* **24**, 221-229.
Kim, S. J., Fernandez-Martinez, J., Sampathkumar, P., Martel, A., Matsui, T., Tsuruta, H., Weiss, T., Shi, Y., Markina-Inarrairaegui, A., Bonanno, J. B. et al. (2014). Integrative structure-function mapping of the nucleoporin Nup133 suggests a conserved mechanism for membrane anchoring of the nuclear pore complex. *Mol. Cell Proteomics* **13**, 2911-2926.
Kupke, T., Di Cecco, L., Müller, H. M., Neuner, A., Adolf, F., Wieland, F., Nickel, W. and Schiebel, E. (2011). Targeting of Nbp1 to the inner nuclear membrane is essential for spindle pole body duplication. *EMBO J.* **30**, 3337-3352.
Laba, J. K., Steen, A. and Veenhoff, L. M. (2014). Traffic to the inner membrane of the nuclear envelope. *Curr. Opin. Cell Biol.* **28**, 36-45.
Liang, B., Dawidowski, D., Ellena, J. F., Tamm, L. K. and Cafiso, D. S. (2014). The SNARE motif of synaptobrevin exhibits an aqueous-interfacial partitioning that is modulated by membrane curvature. *Biochemistry* **53**, 1485-1494.
Liu, Y., Kahn, R. A. and Prestegard, J. H. (2010). Dynamic structure of membrane-anchored Arf*GTP. *Nat. Struct. Mol. Biol.* **17**, 876-881.

Lusk, C. P., Makhnevych, T., Marelli, M., Aitchison, J. D. and Wozniak, R. W. (2002). Karyopherins in nuclear pore biogenesis: a role for Kap121p in the assembly of Nup53p into nuclear pore complexes. *J. Cell Biol.* **159**, 267-278.
Maimon, T., Elad, N., Dahan, I. and Medalia, O. (2012). The human nuclear pore complex as revealed by cryo-electron tomography. *Structure* **20**, 998-1006.
Makhnevych, T., Lusk, C. P., Anderson, A. M., Aitchison, J. D. and Wozniak, R. W. (2003). Cell cycle regulated transport controlled by alterations in the nuclear pore complex. *Cell* **115**, 813-823.
Makio, T., Stanton, L. H., Lin, C. C., Goldfarb, D. S., Weis, K. and Wozniak, R. W. (2009). The nucleoporins Nup170p and Nup157p are essential for nuclear pore complex assembly. *J. Cell Biol.* **185**, 459-473.
Marelli, M., Lusk, C. P., Chan, H., Aitchison, J. D. and Wozniak, R. W. (2001). A link between the synthesis of nucleoporins and the biogenesis of the nuclear envelope. *J. Cell Biol.* **153**, 709-724.
Marfori, M., Mynott, A., Ellis, J. J., Mehdi, A. M., Saunders, N. F., Curmi, P. M., Forwood, J. K., Bodén, M. and Kobe, B. (2011). Molecular basis for specificity of nuclear import and prediction of nuclear localization. *Biochim. Biophys. Acta* **1813**, 1562-1577.
Maurer, P., Redd, M., Solsbacher, J., Bischoff, F. R., Greiner, M., Podtelejnikov, A. V., Mann, M., Stade, K., Weis, K. and Schlenstedt, G. (2001). The nuclear export receptor Xpo1p forms distinct complexes with NES transport substrates and the yeast Ran binding protein 1 (Yrb1p). *Mol. Biol. Cell* **12**, 539-549.
Meinema, A. C., Laba, J. K., Hapsari, R. A., Otten, R., Mulder, F. A., Kralt, A., van den Bogaart, G., Lusk, C. P., Poolman, B. and Veenhoff, L. M. (2011). Long unfolded linkers facilitate membrane protein import through the nuclear pore complex. *Science* **333**, 90-93.
Nath, S., Dancourt, J., Shteyn, V., Puente, G., Fong, W. M., Nag, S., Bewersdorf, J., Yamamoto, A., Antonny, B. and Melia, T. J. (2014). Lipidation of the LC3/GABARAP family of autophagy proteins relies on a membrane-curvature-sensing domain in Atg3. *Nat. Cell Biol.* **16**, 415-424.
Onischenko, E., Stanton, L. H., Madrid, A. S., Kieselbach, T. and Weis, K. (2009). Role of the Ndc1 interaction network in yeast nuclear pore complex assembly and maintenance. *J. Cell Biol.* **185**, 475-491.
Patel, S. S. and Rexach, M. F. (2008). Discovering novel interactions at the nuclear pore complex using bead halo: a rapid method for detecting molecular interactions of high and low affinity at equilibrium. *Mol. Cell. Proteomics* **7**, 121-131.
Pranke, I. M., Morello, V., Bigay, J., Gibson, K., Verbavatz, J. M., Antonny, B. and Jackson, C. L. (2011). α-Synuclein and ALPS motifs are membrane curvature sensors whose contrasting chemistry mediates selective vesicle binding. *J. Cell Biol.* **194**, 89-103.
Ptak, C. and Wozniak, R. W. (2014). Assessing regulated nuclear transport in Saccharomyces cerevisiae. *Methods Cell Biol.* **122**, 311-330.
Söding, J., Biegert, A. and Lupas, A. N. (2005). The HHpred interactive server for protein homology detection and structure prediction. *Nucleic Acids Res.* **33**, W244-W248.
Straube, K., Blackwell, J. S., Jr and Pemberton, L. F. (2010). Nap1 and Chz1 have separate Htz1 nuclear import and assembly functions. *Traffic* **11**, 185-197.
Terry, L. J. and Wente, S. R. (2009). Flexible gates: dynamic topologies and functions for FG nucleoporins in nucleocytoplasmic transport. *Eukaryot. Cell* **8**, 1814-1827.
Timney, B. L., Tetenbaum-Novatt, J., Agate, D. S., Williams, R., Zhang, W., Chait, B. T. and Rout, M. P. (2006). Simple kinetic relationships and nonspecific competition govern nuclear import rates in vivo. *J. Cell Biol.* **175**, 579-593.
Tollervey, D., Lehtonen, H., Carmo-Fonseca, M. and Hurt, E. C. (1991). The small nucleolar RNP protein NOP1 (fibrillarin) is required for pre-rRNA processing in yeast. *EMBO J.* **10**, 573-583.
Tran, E. J., Bolger, T. A. and Wente, S. R. (2007). SnapShot: nuclear transport. *Cell* **131**, 420.
Vollmer, B., Schooley, A., Sachdev, R., Eisenhardt, N., Schneider, A. M, Sieverding, C., Madlung, J., Gerken, U., Macek, B. and Antonin, W. (2012). Dimerization and direct membrane interaction of Nup53 contribute to nuclear pore complex assembly. *EMBO J.* **31**, 4072-4084.
West, M., Zurek, N., Hoenger, A. and Voeltz, G. K. (2011). A 3D analysis of yeast ER structure reveals how ER domains are organized by membrane curvature. *J. Cell Biol.* **193**, 333-346.
White, S. H., Wimley, W. C., Ladokhin, A. S. and Hristova, K. (1998). Protein folding in membranes: determining energetics of peptide-bilayer interactions. *Methods Enzymol.* **295**, 62-87.
Wieprecht, T., Apostolov, O., Beyermann, M. and Seelig, J. (1999). Thermodynamics of the alpha-helix-coil transition of amphipathic peptides in a membrane environment: implications for the peptide-membrane binding equilibrium. *J. Mol. Biol.* **294**, 785-794.
Wozniak, R. W. and Blobel, G. (1992). The single transmembrane segment of gp210 is sufficient for sorting to the pore membrane domain of the nuclear envelope. *J. Cell Biol.* **119**, 1441-1449.
Zhang, D. and Oliferenko, S. (2014). Tts1, the fission yeast homologue of the TMEM33 family, functions in NE remodeling during mitosis. *Mol. Biol. Cell* **25**, 2970-2983.